

## Two-dimensional palladium diselenide for the oxygen reduction reaction

Koh, See Wee; Hu, Jie; Hwang, Jeemin; Yu, Peng; Sun, Zixu; Liu, Qiunan; Hong, Wei; Ge, Junyu; Fei, Jipeng; Han, Byungchan; Liu, Zheng; Li, Hong

2021

Koh, S. W., Hu, J., Hwang, J., Yu, P., Sun, Z., Liu, Q., Hong, W., Ge, J., Fei, J., Han, B., Liu, Z. & Li, H. (2021). Two-dimensional palladium diselenide for the oxygen reduction reaction. *Materials Chemistry Frontiers*, 5(13), 4970-4980. <https://dx.doi.org/10.1039/d0qm01113d>

<https://hdl.handle.net/10356/153163>

<https://doi.org/10.1039/d0qm01113d>

---

© 2021 The Royal Society of Chemistry and the Chinese Chemical Society. All rights reserved. This paper was published in *Materials Chemistry Frontiers* and is made available with permission of The Royal Society of Chemistry and the Chinese Chemical Society.

*Downloaded on 09 Apr 2024 19:16:12 SGT*

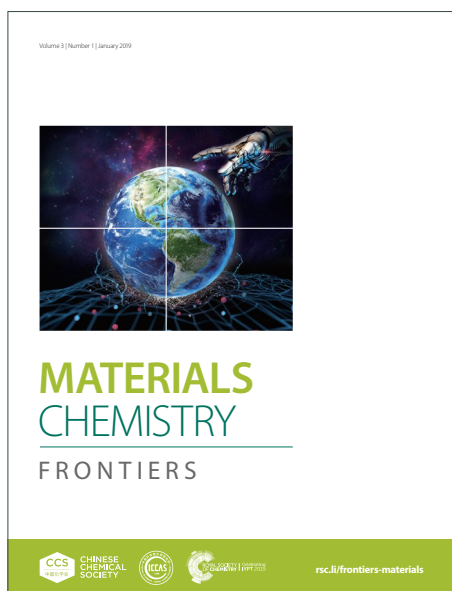
# MATERIALS CHEMISTRY

## FRONTIERS

Accepted Manuscript



This article can be cited before page numbers have been issued, to do this please use: S. W. Koh, J. Hu, J. Hwang, P. Yu, Z. Sun, Q. Liu, H. Wei, J. Ge, J. Fei, B. Han, Z. Liu and H. Li, *Mater. Chem. Front.*, 2021, DOI: 10.1039/D0QM01113D.



This is an Accepted Manuscript, which has been through the Royal Society of Chemistry peer review process and has been accepted for publication.

Accepted Manuscripts are published online shortly after acceptance, before technical editing, formatting and proof reading. Using this free service, authors can make their results available to the community, in citable form, before we publish the edited article. We will replace this Accepted Manuscript with the edited and formatted Advance Article as soon as it is available.

You can find more information about Accepted Manuscripts in the [Information for Authors](#).

Please note that technical editing may introduce minor changes to the text and/or graphics, which may alter content. The journal's standard [Terms & Conditions](#) and the [Ethical guidelines](#) still apply. In no event shall the Royal Society of Chemistry be held responsible for any errors or omissions in this Accepted Manuscript or any consequences arising from the use of any information it contains.

# Two-Dimensional Palladium Diselenide for Oxygen Reduction Reaction

See Wee Koh<sup>1,†</sup>, Jie Hu<sup>1,2,†</sup>, Jeemin Hwang<sup>3,†</sup>, Peng Yu<sup>4,†</sup>, Zixu Sun<sup>1</sup>, Qiunan Liu<sup>5</sup>, Wei Hong<sup>1</sup>, Junyu Ge<sup>1</sup>, Jipeng Fei<sup>1</sup>, Byungchan Han<sup>3,\*</sup>, Zheng Liu<sup>6,\*</sup>, Hong Li<sup>1,7,8\*</sup>

<sup>1</sup>School of Mechanical and Aerospace Engineering, Nanyang Technological University, 639798, Singapore

<sup>2</sup>State Key Laboratory of Metastable Materials Science and Technology, Yanshan University, Qinhuangdao 066004, P. R. China.

<sup>3</sup>Department of Chemical and Biomolecular Engineering, Yonsei University, Seoul 03722, Republic of Korea

<sup>4</sup>State Key Laboratory of Optoelectronic Materials and Technologies, School of Materials Science and Engineering, Sun Yat-sen University, Guangzhou 510275, People's Republic of China.

<sup>5</sup>Nano Energy Center, State Key Laboratory of Metastable Materials Science and Technology, Yanshan University, Qinhuangdao 066004, P. R. China

<sup>6</sup>School of Material Sciences and Engineering, Nanyang Technological University, 639798, Singapore

<sup>7</sup>CINTRA CNRS/NTU/THALES, UMI 3288, Research Techno Plaza, 637553, Singapore

<sup>8</sup>Centre for Micro-/Nano-electronics (NOVITAS), School of Electrical and Electronic Engineering, Nanyang Technological University, 639798, Singapore

\*corresponding authors. E-mail: [bchan@yonsei.ac.kr](mailto:bchan@yonsei.ac.kr); [z.liu@ntu.edu.sg](mailto:z.liu@ntu.edu.sg); [ehongli@ntu.edu.sg](mailto:ehongli@ntu.edu.sg)

†These authors contributed equally to this work.

## Keywords

Two-dimensional catalyst; Palladium diselenide; Electrochemical intercalation; Oxygen reduction; Selenium vacancy; DFT calculation

## Abstract

View Article Online  
DOI: 10.1039/D0QM01113D

The emerging two-dimensional (2D) materials, particularly 2D transition metal dichalcogenides (TMDs), show great potential for catalysis due to their extraordinary large surface areas and tuneable activities. However, the as-synthesized TMDs are usually chemically inert because of their perfect atomic structure and inaccessible interlayer space for electrolytes. Herein, we activate 2D palladium diselenide ( $\text{PdSe}_2$ ) for catalysing oxygen reduction reaction using a controllable electrochemical intercalation process. The electrochemically activated  $\text{PdSe}_2$  exhibits greatly enhanced electrocatalytic activities such as the doubled current density, 250-mV positive shift of potential, 5 times smaller Tafel slope, and greatly improved stability. DFT calculations were employed to study the mechanisms of electrochemical activation. Complementary experimental and theoretical studies suggest that the significantly increased activities come from (1) the activated surface with enriched Se vacancies and chemically bonded oxygen, and (2) easy access of interlayer space for intermediates. Furthermore, the robustness of the Pd-Se bonding ensures high structural stability and excellent resistance to degradation.

## Introduction

Oxygen reduction reaction (ORR) has wide application ranging from metal-air batteries to fuel cells. Typically, precious metals platinum (Pt)-based materials are used as the electrocatalysts, however, the high cost and scarcity of these precious metals are hindering their widespread implementation. Methods to reduce the usage of precious metals without compromising the catalytic activity are highly desirable.<sup>1</sup> A facile and effective way is to mix precious metals with nonprecious elements, *e.g.*, Pt mixed with carbon black.<sup>2</sup> Another effective way is to forming precious metal alloy or compound, *e.g.*, Pt<sub>3</sub>M alloys (M = Ni, Co, Fe, V, Ti, Sc, Y) show high ORR activity with significantly lowered Pt loading.<sup>3-8</sup> Newly developed strategy is to introduce phosphorus (P) into the precious metal to reduce the precious metal loading such as RuP<sub>2</sub>,<sup>9</sup> IrP<sub>2</sub>,<sup>10</sup> and the most recent PtP<sub>2</sub>.<sup>11</sup> By introducing P, the mass activity of PtP<sub>2</sub> had seen significant improvement for ORR in alkaline medium. Alternative to Pt, another superior ORR catalyst, palladium (Pd) has also been extensively studied.<sup>12-14</sup> Being more abundant than Pt, Pd could serve as a perfect alternative to Pt. Phosphor (P)-doped Pd exhibits very high catalytic activity owing to its amorphous structure.<sup>15</sup><sup>16</sup> Electrodeposited palladium–gold (PdAu) alloys also show excellent performances in both acidic and basic medias.<sup>17-19</sup>

The emerging 2D materials, particularly transition metal dichalcogenides (TMDs), represent a new family of candidates for catalysis.<sup>20-22</sup> 2D materials have atomic-thick layer as their basic unit cell, which could maximize the exposure of atoms to its surroundings, and thus maximize the catalyst surface with the same amount of material

used. Moreover, 2D materials have much better stabilities than other nanomaterials of similar sizes as their surfaces are free of dangling bonds.<sup>23-27</sup> Palladium diselenide (PdSe<sub>2</sub>) is a Pd-based 2D TMD that is potentially a promising electrocatalyst due to its excellent electrical conductivity and containing Pd.<sup>28, 29</sup> Moreover, the mass of Pd in PdSe<sub>2</sub> is 60% lower than that of pure Pd metal, implying lower Pd loading for electrocatalysis. Monolayer PdSe<sub>2</sub> has recently been exfoliated from its bulk crystals and shows excellent electrical conductivity and stability in air.<sup>29, 30</sup> 2D PdSe<sub>2</sub> has been employed to catalyse water-splitting,<sup>31</sup> and the PdSe<sub>2</sub> crystal prepared at high-temperature shows excellent electrical properties but limited catalytic activity, due to its perfect crystallinity (*i.e.*, free of defects) and inaccessible interlayer space. Generally, strategies to activate 2D catalysts include: (1) creating vacancies/defects,<sup>32-34</sup> (2) applying elastic strain,<sup>35</sup> and (3) doping or alloying.<sup>32, 36-39</sup> One of the unique properties of 2D layered materials is that their layered geometry allows guest species, *e.g.*, lithium (Li), sodium, magnesium, copper, *etc.*,<sup>40-43</sup> to be inserted between the layers via intercalation to alter the physical and chemical properties of the pristine materials.

Herein, we employ electrochemical intercalation process to activate PdSe<sub>2</sub> for ORR catalysis. Li ions are controllably inserted and extracted from the PdSe<sub>2</sub> crystal *in situ* without modifying the electrode morphology or the phase of the material. The activated PdSe<sub>2</sub> shows greatly improved electrocatalytic activity including more than 100% increase in current density, 250-mV positive shift of potential, and 5 times decrease in Tafel slope. Though typically there is a trade-off between activity and stability of catalyst because high activity indicate stronger chemical interaction between reaction

intermediates and catalyst surface, it is noted that the stability is also greatly enhanced, attributed to the sustained  $2L$  phase<sup>29</sup>, which is different from other TMD electrocatalysts that experience a  $2H$ -to- $1T$  phase change during intercalation.<sup>44-46</sup> With the complementary theoretical modelling, the electrochemical activation of  $\text{PdSe}_2$  ORR catalyst is attributed to two factors: (1) the electric potential-forced Li insertion/extraction creates defects that facilitate the adsorption of oxygen molecules, and (2) the intercalation process increases the interlayer distance and makes much more surface accessible for oxygen species.

## Experimental

### Synthesis of intercalated $\text{PdSe}_2$ (I- $\text{PdSe}_2$ )

Bulk  $\text{PdSe}_2$  single crystals were grown by a self-flux method through melting stoichiometric amounts of Pd powder and Se powder.<sup>29</sup> I- $\text{PdSe}_2$  was obtained by activating  $\text{PdSe}_2$  via electrochemical intercalation with lithium hexafluorophosphate, as schematically illustrated in **Fig. S1**. A certain amount  $\text{PdSe}_2$  and polyvinylidene fluoride (PVDF) were dispersed in 10 ml NMP and ultrasonicated for 24 h (the ratio of  $\text{PdSe}_2$ : PVDF was 9:1), and then coated on copper foil to about 3cm by 4cm. The sample was then attached to a Land Battery tester in argon atmosphere to perform the intercalation. After which, the sample was removed from the copper foil through a few rounds of ultrasonication and centrifugation. The sample preparation method was repeated with intercalation current (current density) of 25  $\mu\text{A}$  ( $2.08 \mu\text{A cm}^{-2}$ ), 50  $\mu\text{A}$  ( $4.17 \mu\text{A cm}^{-2}$ ) and 100  $\mu\text{A}$  ( $8.33 \mu\text{A cm}^{-2}$ ), where the samples were denoted as I- $\text{PdSe}_2$ -

25, I-PdSe<sub>2</sub> and I-PdSe<sub>2</sub>-100, respectively.

View Article Online  
DOI: 10.1039/D0QM01113D

### Physical Characterization

The crystal phase and structure were examined by X-ray diffraction (XRD, Panalytical Xpert Pro) with Cu K $\alpha$  ( $\lambda=0.15406$  nm) radiation in the range of 10–90°. Raman spectra were obtained using a WITec CRM200 confocal Raman microscopy system with the excitation line of 488 nm. The morphology of the samples was examined by transmission electron microscopy (TEM, JEOL-2010) at an acceleration voltage of 200 KV. X-ray photoelectron spectroscopic (XPS) measurements were performed on a Kratos AXIS Supra with an Al K $\alpha$  source ( $h\nu=1486.6$  eV).

### Electrochemical measurements

Electrochemical measurements were carried out with a conventional three-electrode system on an electrochemical workstation (Gamry Potentiostat Reference 600) at room temperature. Platinum wire and Ag/AgCl (Saturated KCl) electrode were used as the auxiliary and reference electrodes, respectively. All potentials in this study were given versus reversible hydrogen electrode (RHE) according to the following equation

$$E(RHE) = E(Ag/AgCl) + 0.059 \times pH + 0.198$$

The working electrode was prepared as follows: 4 mg of material (the ratio of the as-prepared catalyst: acetylene black was 1:1) and 12  $\mu$ L of Nafion solution (5 wt.%) were dispersed in 2 mL isopropanol solution by sonication for 30 min. Then, 25  $\mu$ L of



the catalyst ink was dropped on the glassy carbon electrode surface ( $D = 5 \text{ mm}$ ). For comparison, the commercial Pt/C (20 wt % Pt, Alpha Aesar) catalyst ink was prepared by following the same procedure.

A rotating disk electrode (RDE) measurement was performed in  $\text{O}_2$ -saturated 0.1 M KOH solution at different rotation rates (400-1600 rpm) with a scan rate of  $5 \text{ mVs}^{-1}$  from -1 V to 0.2 V (vs. Ag/AgCl).

The number of transferred electrons ( $n$ ) calculated from RDE test was based on the Koutecky-Levich (K-L) equation:

$$I_d^{-1} = i_{dl}^{-1} + i_k^{-1} = \left( B \omega^{\frac{1}{2}} \right)^{-1} + i_k^{-1}$$

$$B = 0.62nFCo(D\omega)^{\frac{2}{3}}\nu^{-\frac{1}{6}}$$

where  $i_d$  is the measured current density,  $i_{dl}$  and  $i_k$  are the kinetic and film diffusion-limiting current densities, and  $B$  is the reciprocal of the slope,  $\omega$  is the angular velocity of the disk ( $\omega = 2\pi N$ , where  $N$  is the linear rotation speed),  $n$  is the number of electrons in oxygen reduction,  $F$  is the Faraday constant ( $96500 \text{ C} \cdot \text{mol}^{-1}$ ),  $Co$  is  $\text{O}_2$  volume concentration in 0.1 M KOH ( $1.14 \times 10^{-6} \text{ mol} \cdot \text{cm}^{-3}$ ),  $\nu$  is the kinematic viscosity of the electrolyte ( $0.01 \text{ cm}^2 \cdot \text{s}^{-1}$ ), and  $Do$  is the diffusion coefficient of  $\text{O}_2$  in 0.1 M KOH ( $1.73 \times 10^{-5} \text{ cm}^2 \cdot \text{s}^{-1}$ ).

Tafel slope was calculated according to Tafel equation:

$$E = a + b \log(j_k)$$

where  $E$  is the applied potential in the LSV test,  $a$  is a constant,  $b$  is the Tafel slope and  $j_k$  is the kinetic current density.

The electrochemically active surface areas (ECSA) were estimated from the electrochemical double-layer capacitance ( $Cdl$ ) by collecting cyclic voltammograms (CV) in a non-Faradaic region of 1.06 – 1.16 V vs RHE following the equation

$$ECSA = \frac{Cdl}{Cdl_{ref}}$$

where  $Cdl$  is the double layer capacitance measured by CV scan in non-Faradaic potential window. The reference  $Cdl_{ref}$  is typically around 20 to 80  $\mu F \cdot cm^{-2}$ ,<sup>47, 48</sup> and thus we adopted the  $Cdl_{ref}$  around the middle value of 60  $\mu F \cdot cm^{-2}$  which is consistent with that of reported precious metals including Pd.<sup>49-51</sup>

The CV tests were recorded over an applied potential range of 1.06 to 1.17 V vs RHE. The potential range is constant for all catalysts and the same scan rates of 40, 60, 80, and 100  $mV s^{-1}$  were selected.

### Calculation methods

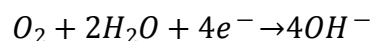
The density function theory (DFT) calculations were performed by Vienna Ab-initio Simulation Package (VASP).<sup>52</sup> The exchange-correlation energy functional was described within the generalized gradient approximation (GGA)<sup>53</sup> in the Perdew-Burke-Ernzerhof (PBE) functional.<sup>54</sup> The projector augmented wave (PAW)<sup>55</sup> potentials were used with a 520 eV cut-off energy and the Brillouin zone integration was sampled by a  $3 \times 3 \times 1$  k-grid mesh for a unit cell. The van der Waals interactions were described by DFT-D2 approach of Grimme<sup>56</sup> and spin polarization effect was considered. The convergence criteria for the energy and force were set to  $1 \times 10^{-5}$  eV and 0.02 eV/Å, respectively.

The defect formation energy ( $E_f$ ) of Se was calculated using following equation:

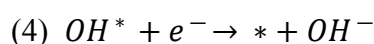
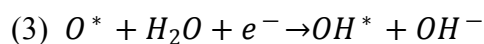
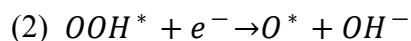
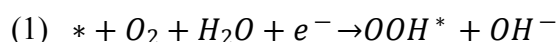
$$E_f = E_D - E_P + N_{Se}\mu_{Se}$$

where  $E_D$  and  $E_P$  are the calculated ground state energy of defected and pristine model, respectively;  $N_{Se}$  corresponds to the number of defected Se atoms;  $\mu_{Se}$  represents the chemical potential of Se which was obtained from bulk octaselenium ring structure.

The overall reaction of  $O_2$  reduction to  $OH^-$  in alkaline media is as follows:



To examine ORR performance, following associative mechanism with the four-electron reaction pathway is considered in the calculations:



The sign \* refers to an active site on the catalyst models. The Gibbs free energy of adsorption is calculated by following equation:

$$\Delta G = \Delta E + \Delta ZPE - T\Delta S + \Delta G_U + \Delta G_{pH} + \Delta G_w$$

where  $\Delta E$  is the adsorption energy which can be directly obtained from the calculations;  $\Delta ZPE$  is the zero point energy corrections and  $\Delta S$  is the vibrational entropy contribution at room temperature ( $T = 298.15 \text{ K}$ )<sup>31</sup>;  $\Delta G_U = -eU$ , where  $U$  is the electrode potential;  $\Delta G_{pH}$  is the correction of the  $H^+$  free energy where  $\Delta G_{pH} = -k_B T \ln(10) \times pH$  ( $k_B$  is Boltzmann's constant and  $pH = 13$ );  $\Delta G_w$  is the

stabilization energy by water molecules calculated by implicit solvation model.<sup>57</sup> The free energy of O<sub>2</sub> was derived from  $G_{O_2} = 2G_{H_2O(l)} - 2G_{H_2} + 4.92 \text{ eV}$ . The free energy of H<sub>2</sub>O<sub>(g)</sub> and H<sub>2</sub> was calculated in the gas phase at room temperature. The free energy of H<sub>2</sub>O<sub>(l)</sub> was calculated by  $G_{H_2O(l)} = G_{H_2O(g)} + RT * \ln(\frac{p}{p_0})$ , where R is the ideal gas constant, T = 298.15 K, p = 0.035 bar, and p<sub>0</sub> = 1 bar.

The overpotential was calculated by  $\eta_{RHE} = 1.23 - \max[\Delta G_1, \Delta G_2, \Delta G_3, \Delta G_4]$ . Free energy changes of each reaction step are shown in **Table S1**.

## Results and discussion

The schematic PdSe<sub>2</sub> before (pristine) and after the electrochemical activation process (I-PdSe<sub>2</sub>) is illustrated in **Fig. S1**. When the as-prepared PdSe<sub>2</sub> is subjected to the Li intercalation forced by an electric potential, the interlayer distance increases due to the relatively larger diameter of Li ion compared to the van der Waal gap. This expands the volume of the crystal, and thus allows the diffusion of the ions between layers and encourages oxygen diffusion into the interlayer space.<sup>58</sup> Subsequently, the chemically active parts of the crystal, *e.g.*, the edge, grain boundaries, are activated by the reactive and energetic Li ions, and structure defects such as Se vacancies are created. X-ray diffraction (XRD) and Raman spectroscopy were performed to establish the crystal structure, as shown in **Fig. 1a** and **Fig. 1b**, respectively. Despite the lithiation process, the XRD shows that the major PdSe<sub>2</sub> peaks have been retained after intercalation, suggesting similar crystallinity. It is noted that there is no obvious shift of the (002) peaks at 23.1° but an overall change of 0.1 degree (**Table S2**), suggesting

that the interlayer spacing increment is small after de-lithiation, which is crucial to maintaining the electrode integrity after activation process. However, the presence of newly formed bump on the left the (002) peak evidently suggests strain broadening of the lattice which can be attributed to the intercalated foreign species that could have been lodged in between the plane.<sup>59</sup> The lodged molecules in this case could have contributed to exposing the interplanar layers to increase activity through improved oxygen diffusion<sup>60</sup> as evident from the improvement of electrochemical surface area (ECSA), which will be discussed later. The Raman spectrum in **Fig. 1b** shows negligible change of peak position or width, suggesting no dramatic chemical composition/structure change has occurred. The main peaks of PdSe<sub>2</sub> occurs around ~143.65, 206.62, 222.27 and 257.32 cm<sup>-1</sup> while that of I-PdSe<sub>2</sub> occurs at ~142.86, 205.06, 220.70 and 256.54 cm<sup>-1</sup>, indicating a redshift which suggests the bond length increasing. This could be attributed to the effect of introducing lithium into the structure that induced strain on the layer<sup>61</sup> and loosening the chemical bond of the structure which is consistent with the XRD characterization.

Transmission electron microscopy (TEM) images in **Fig. S2a** and **S2b** further confirm that there is no obvious difference in morphology between flakes of PdSe<sub>2</sub> and I-PdSe<sub>2</sub>, suggesting the maintaining of structural integrity after activation process.

The high-resolution TEM (HRTEM) image of pristine PdSe<sub>2</sub> (**Fig. 1c**) and the corresponding Fourier transform pattern (Inset of **Fig. 1c**) show high degree of crystallinity with no obvious defects, arising from the high-temperature growth process, which ensures the superior electrical properties. The interlayer spacing is 0.29 nm,

corresponding to the (002) face of  $\text{PdSe}_2$ . The HRTEM image of I- $\text{PdSe}_2$  in **Fig. 1d** confirms the structural integrity and good crystallinity of  $\text{PdSe}_2$  after the activation process. Moreover, the corresponding Fourier transform pattern (inset of **Fig. 1d**) supports the slight variation of crystallinity after the activation.

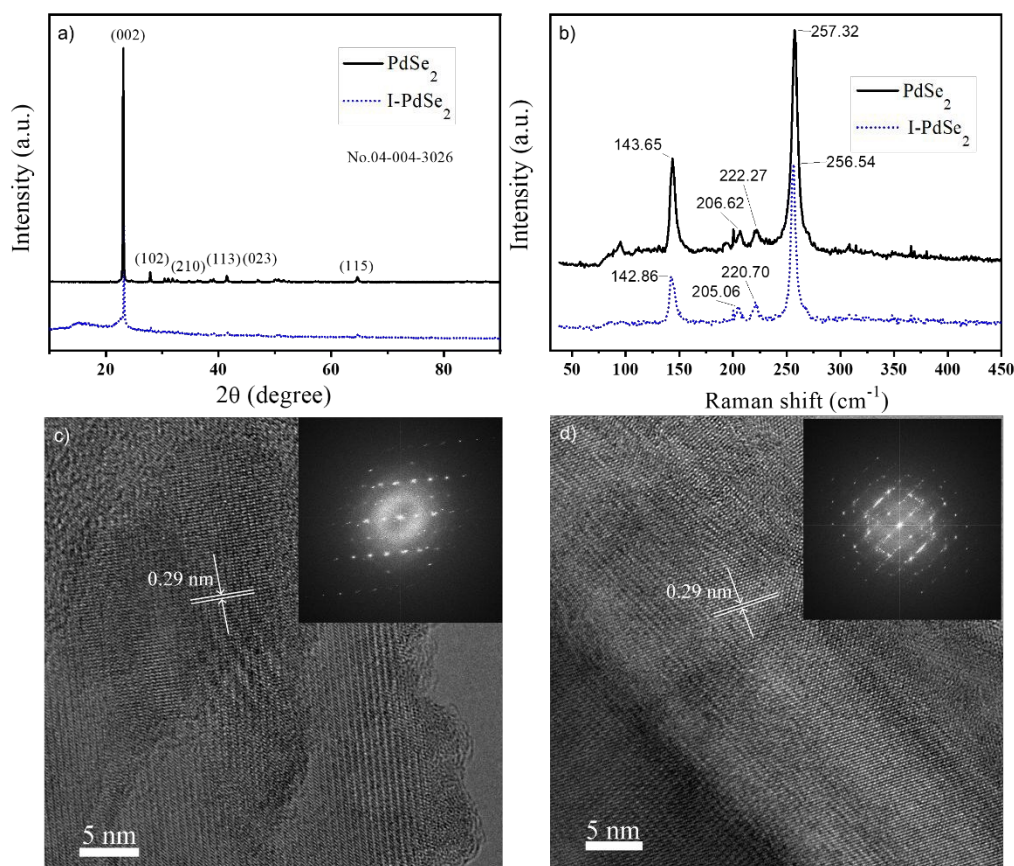


**Fig. 1** Material characterizations. (a) XRD patterns, (b) Raman spectra, (c, d) HRTEM images of  $\text{PdSe}_2$  and I-  $\text{PdSe}_2$ . Insets of (c) and (d): the corresponding Fourier transform patterns.

The detailed chemical composition was further examined by X-ray photoelectron spectroscopy (XPS). No notable difference can be seen in the XPS spectrum before and after activation (**Fig. 2a**), indicating that all the elements and chemical bonds have been preserved in I- $\text{PdSe}_2$  during activation. The emerging F1s peak after intercalation at the

high energy region could come from the residual of intercalation agent (i.e., PDVF) in the sample, which agrees with the new carbon peaks in C 1s spectrum.

The Pd 3d XPS spectrum of PdSe<sub>2</sub> crystal (**Fig. 2b**), exhibits doublet peaks at around 334.5 eV and 339.8 eV, corresponding to the 3d<sub>5/2</sub> and 3d<sub>3/2</sub> components of PdSe<sub>2</sub>, respectively. The minor downshift of Pd peaks in I-PdSe<sub>2</sub> could be caused by the decrease of Pd oxidation state arising from Se vacancies created in the activation process. As suggested in previous report,<sup>29</sup> the Li<sup>+</sup> species could have formed bonds with Se during the lithiation process hence allows the easy dissociation of Se during de-lithiation.

The Se 3d spectrum (**Fig. 2c**) consists of two peaks corresponding to Se 3d<sub>5/2</sub> and 3d<sub>3/2</sub>, respectively, and they tend to merge due to weakening of Se peak intensity, which can be ascribed to Se vacancies formed during intercalation. Fitting of XPS spectra indicates decreasing of Se:Pd ratio from 1.6947 to 1.5867 due to intercalation (**Table S3**), suggesting the loss of Se. Introducing Se vacancies allows ORR intermediates to contact the interlayer Pd more easily. As a precious metal, Pd's high selectivity and affinity to oxygen<sup>62-64</sup> plays a huge part at capturing O<sub>2</sub> for further reduction process as O<sub>2</sub> binds and dissociates readily on Pd.<sup>62</sup> This means that the O-O bonds in the ORR intermediates could actively interact with the newly exposed interlayer Pd.

The O1s spectrum (**Fig. 2d**) was deconvoluted into three peaks located at 530.3, 531.5 and 533 eV, corresponding to the lattice oxygen species, hydroxide species and the surface adsorbed oxygen, respectively.<sup>65</sup> The increase in lattice oxygen in I-PdSe<sub>2</sub> sample, further supports that activation process generated surface vacancies that are



prone to be oxidized. At the same time, the intercalation increased the amount of adsorbed oxygen, suggesting the structure defects created during intercalation have good affinity to oxygen species. And the enhanced affinity to oxygen intermediates can promote catalytic oxygen reduction reaction.

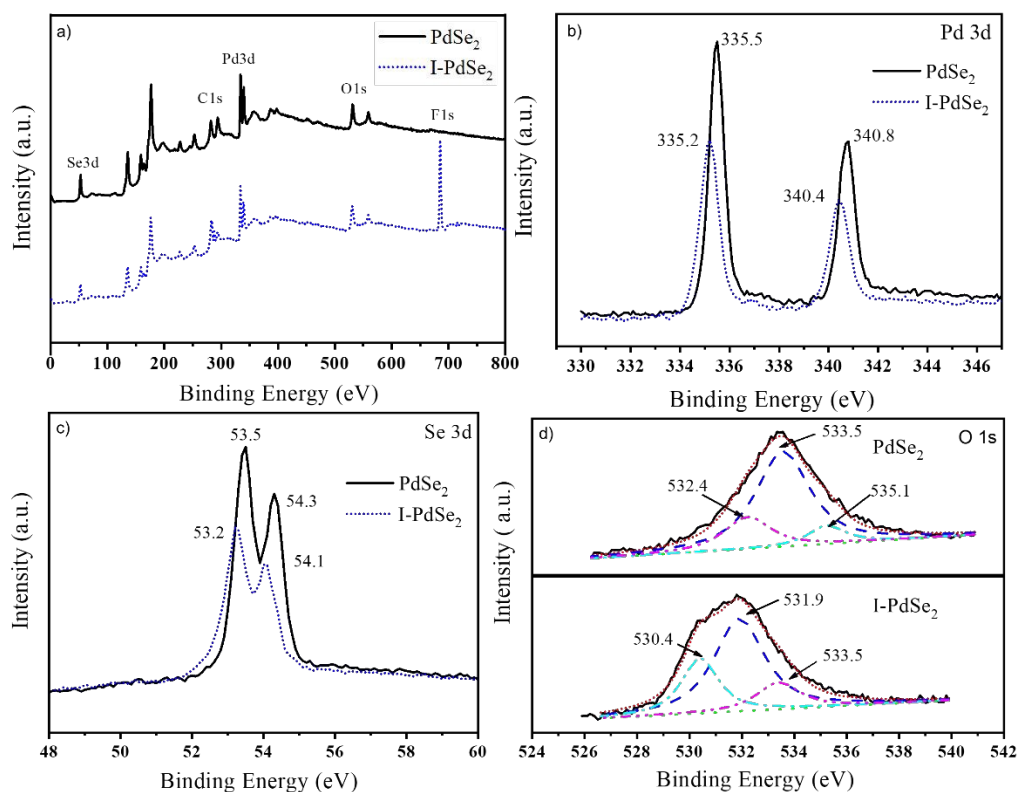


**Fig. 2** XPS characterization. XPS spectra (a) and high-resolution XPS curves of (b) Pd3d, (c) Se3d, and (d) O1s of PdSe<sub>2</sub> and I- PdSe<sub>2</sub>.

**Fig. 3a** shows the LSV curves of PdSe<sub>2</sub>, I-PdSe<sub>2</sub>-25, I-PdSe<sub>2</sub>-50, I- PdSe<sub>2</sub>-100 and commercial 20 wt% Pt/C, where the number at the back signifies the intercalation current applied (in  $\mu\text{A}$ ), and a summary of the performances is presented in **Table S4**. Apparently, I-PdSe<sub>2</sub>-50 exhibits more positive potentials (both onset and half-wave potentials) and larger diffusion-limited current density than PdSe<sub>2</sub>, I-PdSe<sub>2</sub>-25 and I-



PdSe<sub>2</sub>-100, indicating I-PdSe<sub>2</sub>-50 has an optimized ORR activity.

To further unravel the reaction kinetics for ORR, the LSV measurements at 400-1600 rpm were performed, and the kinetic parameters were calculated by Koutecky-Levich (K-L) equation, as shown in **Fig. S3**. The diffusion-limited current densities of different samples show an increasing trend due to the higher rate of diffusion. The fitting K-L plots show linear relationships between  $j^{-1}$  and  $\omega^{-1/2}$  under each potential. The number of transferred electrons  $n$  for I-PdSe<sub>2</sub>-50 was calculated to be 3.67 at different potentials from 0.2 V to 0.6 V (inset of **Fig. S3**), indicating a four-electron dominated transfer pathway for ORR. The higher electron transfer number of I-PdSe<sub>2</sub>-50, than those of I-PdSe<sub>2</sub>-25 and I-PdSe<sub>2</sub>-100, indicates a better suppression of formation of HO<sub>2</sub><sup>-</sup> during the conversion of O<sub>2</sub> into OH<sup>-</sup>, in turn translating to the better performance of ORR conversion since the desired four-electron pathway is dominant.<sup>66</sup>

Optimization at intercalation current density of 4.17  $\mu\text{A cm}^{-2}$ , i.e., current of 50  $\mu\text{A}$ , could be a result of balanced rate of intercalation. A high intercalation current density of 8.33  $\mu\text{A cm}^{-2}$  (current of 100  $\mu\text{A}$ ) decreases the effectiveness of intercalation where the intercalation could be incomplete due to drastic interlayer ion drifting and hence insufficient to expose all interlayer active sites<sup>67</sup>. On the other hand, a low current density of 2.08  $\mu\text{A cm}^{-2}$  (current of 25  $\mu\text{A}$ ) enables a milder intercalation and might have been insufficient to create abundant active sites. Moreover, a slow rate of intercalation could allow the build-up of solid electrolyte interface from the breakdown of electrolyte on the surface of the PdSe<sub>2</sub>,<sup>68, 69</sup> which creates a protective layer that shields the material from defects formation or blocks the active sites.<sup>70</sup>

The corresponding Tafel slope (**Fig. 3b**) of I-PdSe<sub>2</sub>-50 was calculated to be 64 mV dec<sup>-1</sup>, smaller than that of Pt/C (74 mV dec<sup>-1</sup>), suggesting the faster kinetics process than Pt/C. The electrochemical double-layer capacitance ( $C_{dl}$ ) was measured to obtain ECSA. Cyclic voltammetry (CV) was performed to evaluate  $C_{dl}$  and then to calculate the ECSA of various catalysts. The CV curves recorded at different scan rates for all catalysts, and the linear fitting of current density versus scan rate are displayed in **Fig. S4**. The summary of ECSA values is shown in **Fig. 3c**, and I-PdSe<sub>2</sub> has a much greater ECSA than pristine PdSe<sub>2</sub>, confirming that the ORR active sites density has been dramatically increased by intercalation.

Next, we examine the stability of the catalysts. As shown in **Fig. 3d**, I-PdSe<sub>2</sub> exhibits 14.5% decrease after 28800-s continuous operation, showing a much better durability and stability than Pt/C which displays a faster current loss about 35% under the same conditions. The change in half-wave potential and loss of diffusion-limited current density are almost negligible, as shown the **Fig. S5**, further supporting the superior stability of I-PdSe<sub>2</sub>-50. The lack of durability of the Pt/C relative to I-PdSe<sub>2</sub>-50 can be attributed to the loose carbon black constituent in the commercial Pt/C catalyst that leads to easily dissolved Pt particles and aggregation under working conditions.<sup>71</sup> The excellent stability of I-PdSe<sub>2</sub>-50 is attributed to the retained thermodynamically stable 2L phase after intercalation, which is different from 2H-to-1T phase transition caused by Li interaction in other TMD electrocatalysts including molybdenum sulfide, tungsten sulfide etc.<sup>44-46, 58</sup> To benchmark the optimized catalyst I-PdSe<sub>2</sub>, the catalytic performance of some other Pd-based ORR electrocatalysts are

compared in **Table S5**, which shows that I-PdSe<sub>2</sub>-50 is among the best in terms of balanced performance and stability despite the ease of activation process. It is worth noting that, despite the robustness and durability of the material, it is still based on precious metal catalysts, thus it is unable to resist the methanol crossover during ORR process.<sup>72-74</sup>

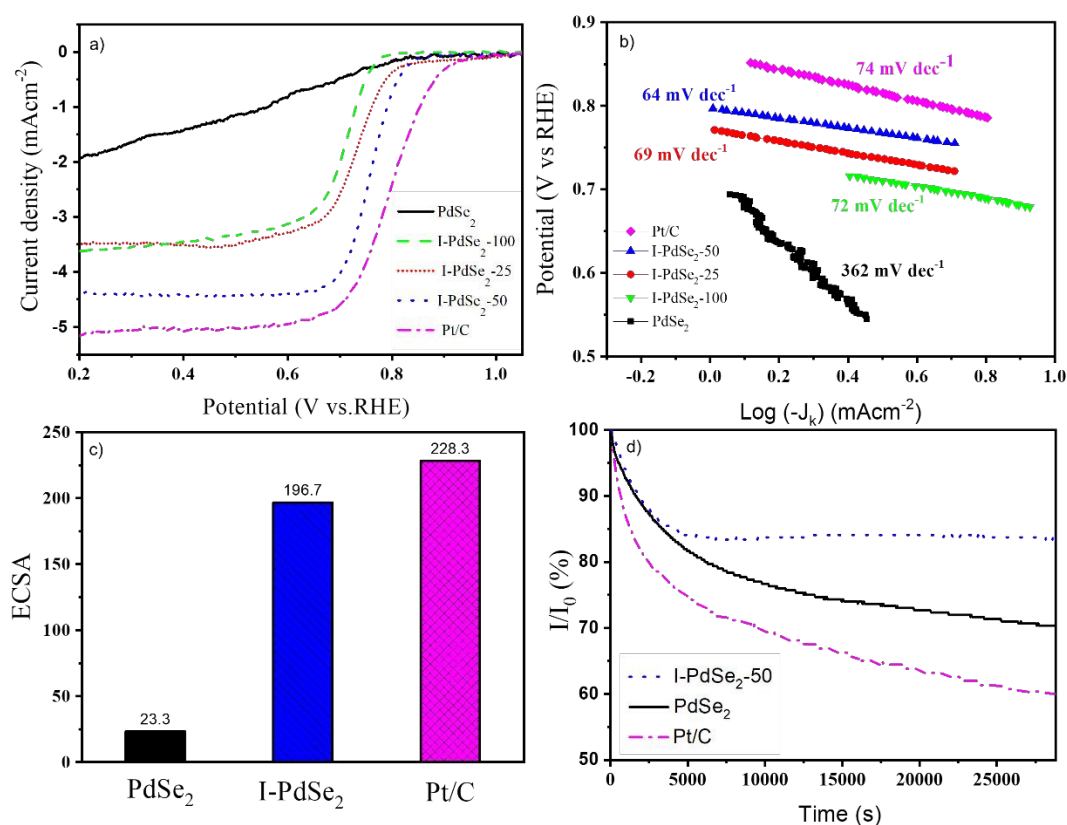


**Fig. 3** Electrochemical performances of PdSe<sub>2</sub>, I-PdSe<sub>2</sub>-25, I-PdSe<sub>2</sub>-50, I-PdSe<sub>2</sub>-100 and Pt/C. (a) ORR polarization curves and (b) corresponding Tafel plots, (c) ECSA, and (d) chronoamperometric curves in O<sub>2</sub>-saturated 0.1 M KOH solution at 400 rpm under a potential of 0.55 V versus RHE.

We further conducted density functional theory (DFT) calculations to evaluate the stability and ORR activity for PdSe<sub>2</sub> and I-PdSe<sub>2</sub>. In our calculations, bulk PdSe<sub>2</sub> structure has lattice parameters of  $a = 5.82 \text{ \AA}$ ,  $b = 5.91 \text{ \AA}$  and  $c = 7.40 \text{ \AA}$ , consistent

with experimental values.<sup>75</sup> For I-PdSe<sub>2</sub> model, the interplanar distance was doubled as depicted in **Fig. S6** to observe the ORR activity between layers. The (001) facets of 2 × 2 supercell for both PdSe<sub>2</sub> and I-PdSe<sub>2</sub> were modelled with periodically repeating 4-layer slab with a vacuum of about 15 Å along the direction normal to the sheet plane to avoid interaction between the periodic images, as shown in **Fig. 4a**. The bottom two layers were fixed in their bulk positions.

To evaluate the stability, the defect formation energy for PdSe<sub>2</sub> and I-PdSe<sub>2</sub> with various defect formation pathways were calculated, as presented in **Fig. 4b**. Since it is well known that defect formation of a Se is more favourable than that of Pd, the models with Se defects were constructed. There are 5 types of defective models as shown in the inset of **Fig. 4b**. Two of them are the models with one Se defect on the first (L1) and the second layer (L2) each. Since there is a high chance that the first Se defect is already formed during de-lithiation, the formation energy of the second Se defect was also analysed to evaluate the stability during ORR process. Therefore, rest of the models have two Se defects, i.e., two defects on the first layer (L1L1), one defect on each layer (L1L2), and two defects on the second layer (L2L2). One can see that I-PdSe<sub>2</sub> shows greater defect formation energy than PdSe<sub>2</sub>, suggesting higher stability against defect formation. To obtain more insights into the Se defect formation energy and the nature of chemical bond between Pd and Se, the defect formation on the surface was examined by Crystal Orbital Hamilton Populations (COHP) analysis, which separates the band structure energy into bonding (negative value), nonbonding, and antibonding (positive value) contributions.<sup>76</sup> As shown in **Fig. S7**, COHP plot of PdSe<sub>2</sub> (black) is positioned

at lower energy than that of I-PdSe<sub>2</sub> (blue) indicating more electrons are involved in Pd-Se bonding because of the covalent-like quasi-bond between layers.<sup>77</sup> As the anti-bonding orbitals are crossing the Fermi energy, more electrons are occupying anti-bonding orbital for PdSe<sub>2</sub> than I-PdSe<sub>2</sub> leading to weaker bond strength. The integrated COHP (ICOHP) in **Table S6**, which summarizes the electrons filled in states up to the Fermi energy in COHP, also indicates Pd-Se bonding in I-PdSe<sub>2</sub> is more stable than that in PdSe<sub>2</sub>. Additionally, bond length between Se and two adjacent Pd are compared in **Table S7**, where I-PdSe<sub>2</sub> has slightly smaller Pd-Se bond length than PdSe<sub>2</sub>, implying stronger bond strength between Pd and Se.

For PdSe<sub>2</sub>, a Se defect formation on the first layer (L1, 1.71 eV) is more difficult than that on the second layer (L2, 1.68 eV). After the formation of the Se defect on the first layer (L1), subsequent Se defect can be formed on both layers with less energy, i.e., the first layer next to the already formed one (L1L1, 1.57 eV) or the second layer (L1L2, 1.58 eV). For the case when a defect is formed on the second layer (L2), it is easier for the second Se defect to be formed on the same layer (L2L2, 1.14 eV) than on the first layer (L2L1, 1.71 eV). The defect formation energy on I-PdSe<sub>2</sub> for L1 (2.21 eV), L1L2 (2.25 eV), L2 (2.24 eV) and L2L1 (2.22 eV) are similar as the interlayer interaction is weaker than that of PdSe<sub>2</sub> due to the larger interlayer distance. The second Se defect forms relatively easier on the layer with existing first defect (L1L1, 2.03 eV; L2L2, 2.05 eV); however, these defect formations are still endothermic which requires high energy to overcome. In other words, even a Se defect is formed during de-lithiation process, the subsequent Se defect formation is still unfavourable which leads to the high

stability of I-PdSe<sub>2</sub>.

Next, we examine the influence of the defect and increased interlayer distance on ORR activity for I-PdSe<sub>2</sub>.<sup>78</sup> As presented in **Fig. 4c**, the Gibbs free energy diagrams on the associative 4e<sup>-</sup> reaction pathways in alkaline medium (pH = 13) were calculated using previously developed method<sup>79</sup> for pristine PdSe<sub>2</sub>, pristine I-PdSe<sub>2</sub>, I-PdSe<sub>2</sub> (L1) and I-PdSe<sub>2</sub> (L2) models. Due to the larger interlayer distance of I-PdSe<sub>2</sub> than that of PdSe<sub>2</sub>, we assumed that O<sub>2</sub> can access interlayer space and the catalytic reaction can occur on the second layer (2L), as shown in **Fig. S8**. Therefore, ORR not only on the first layer (solid line) but also on the second layer (2L, dotted line) of I-PdSe<sub>2</sub> were also presented. The Gibbs free energy diagram exhibits the lowest overall reaction energy change at equilibrium potential ( $U^0$ ), suggesting their theoretical ORR performance. For pristine PdSe<sub>2</sub> (black) and I-PdSe<sub>2</sub> (blue), the rate-determining step is evaluated as the first electron transfer step to form chemisorbed OOH\* from H<sub>2</sub>O ( $\Delta G_1$ ) for both models. The first electron transfer step is the adsorption of OOH which is an endothermic reaction with overpotential of ( $\eta_{RHE}$ ) of 1.58 V for PdSe<sub>2</sub> and 1.71 V for I-PdSe<sub>2</sub>. The rate-determining steps are determined as the first electron transfer step for all but two models. The two exceptions are the I-PdSe<sub>2</sub> with a defect on the first layer (I-PdSe<sub>2</sub> (L1)) and I-PdSe<sub>2</sub> with a defect on the second layer whose active site is also on the second layer (I-PdSe<sub>2</sub> (L2\_2L)). I-PdSe<sub>2</sub> (L1) and I-PdSe<sub>2</sub> (L2\_2L) show high ORR performance with different rate-determining step, the third electron transfer step ( $\Delta G_3$ ) where overpotential is 0.98 eV and 1.14 eV, respectively. These two models are the ones that intermediates adsorbed on the defect site. The defect increases the

adsorption energy of OOH which changes the rate-determining step and decreases the overpotential of ORR. The ORR overpotentials on the I-PdSe<sub>2</sub> are similar or smaller to those of the PdSe<sub>2</sub> indicating the surface area with similar or better activity compared to PdSe<sub>2</sub> have increased for I-PdSe<sub>2</sub>. Therefore, one can conclude that the conversion from PdSe<sub>2</sub> to I-PdSe<sub>2</sub> activates the ORR by enriched and diversified active sites. Also, defects on I-PdSe<sub>2</sub> improve the ORR activity by tuning electronic structure.<sup>80</sup>

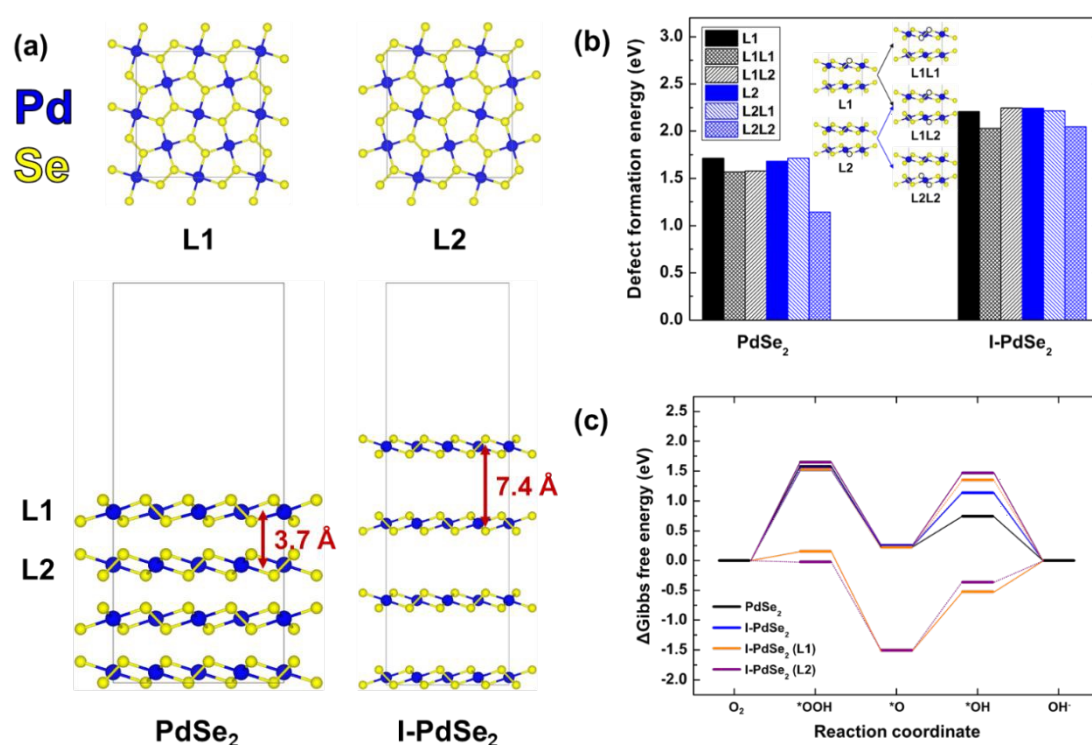


**Fig.4** (a) Model systems of PdSe<sub>2</sub> and I-PdSe<sub>2</sub>. (Pd: blue, Se: yellow). The top view of the first (L1) and second (L2) layer and the lateral views of PdSe<sub>2</sub>, I-PdSe<sub>2</sub>. (b) Defect formation energy for each defective models. Insets: The corresponding schematic models of 5 different defect types. (c) Gibbs free energy of the oxygen reduction reaction (ORR) at equilibrium potential ( $U^0$ ) for pristine and defective models with various active sites.

The strategy employed in this work shows that 2D crystals with robust phase can

be achieved with the development of more controllable in situ intercalation method, e.g., mild intercalation process that allows one to fine tune the activity and stability of 2D catalyst, without damaged or drastic phase/structural changes during intercalation which is highly desirable. Therefore, exploring of in situ characterization tools to monitor the evolution of activity and stability during intercalation is crucial for reaching optimal balance between activity and stability.

## Conclusion

2D PdSe<sub>2</sub> has been activated for ORR catalysis using lithium intercalation. The good crystallinity and 2L phase of pristine PdSe<sub>2</sub> are well retained, offering the greatly enhanced activity as well as superior stability. The de-lithiation process forces weak Pd-Se bonding to dissociate to create active sites by exposing more Pd element. Furthermore, the lithiation process introduces intercalation that improves the oxygen diffusion. Our complementary DFT calculation indicates Li-intercalation induces active sites that enhance ORR activity. Furthermore, the high bond energy between Pd and Se beneath the surface layers ensures that further defect formation is unfavourable, giving it superior stability. These complementary experimental and theoretical studies indicate that lithiation/de-lithiation cycle can activate PdSe<sub>2</sub> for ORR without significantly degrading the original good crystallinity of PdSe<sub>2</sub> synthesized at high temperature, in obvious contrast to the lithium intercalation of other TMD electrocatalysts where stable 2H phase is usually converted to metastable 1T phase accompany with structural defects. The immediate benefit of the retained crystallinity



and stable phase is the greatly enhanced activity without compromising stability, which could effectively address the activity-stability dilemma in electrocatalysts.

## Author Contributions

S.W.K., J.H. and H.L. conceived the idea and designed the experiments. P.Y. and Z.L. performed material preparation. J.H., S.W.K. and Z.S. performed electrochemical measurements and collected data. S.W.K., J.G. and Q.L. performed the material characterizations. W.H., J.F. assisted in the electrochemical measurements. J.H. and B.H. performed DFT calculation. J.H., S.W.K., J.H. and Y.P. wrote the manuscript, and all authors discussed the results.

## Acknowledgements

This work was supported by Nanyang Technological University under NAP award (M408050000) and Singapore Ministry of Education Tier 1 program (2018-T1-001-051). J.H. is grateful for financial support from the National Natural Science Foundation of China (Nos.51771165 and 51925105), the Natural Science Foundation of Hebei Province (No. E2020203123). B.H. acknowledges the support from the Global Frontier Program through the Global Frontier Hybrid Interface Materials (GFHIM) of the NRF funded by the Ministry of Science and ICT (Project No. 2013M3A6B1078882).

## Conflict of Interest

The authors declare that they have no known competing financial interests or personal relationships that could have appeared to influence the work reported in this paper.

## References

1. W. Hong, C. Guo, S. W. Koh, J. Ge, Q. Liu, W. Tu, M. Yao, Z. Sun, J. Xiao and H. Li, One-dimensional metal-organic nanowires-derived catalyst of carbon nanobamboos with encapsulated cobalt nanoparticles for oxygen reduction, *Journal of Catalysis*, 2020, DOI: <https://doi.org/10.1016/j.jcat.2020.10.030>.
2. Z. A. C. Ramli and S. K. Kamarudin, Platinum-Based Catalysts on Various Carbon Supports and Conducting Polymers for Direct Methanol Fuel Cell Applications: a Review, *Nanoscale Res. Lett.*, 2018, **13**, 410.
3. J. Greeley, I. E. L. Stephens, A. S. Bondarenko, T. P. Johansson, H. A. Hansen, T. F. Jaramillo, J. Rossmeisl, I. Chorkendorff and J. K. Nørskov, Alloys of platinum and early transition metals as oxygen reduction electrocatalysts, *Nat. Chem.*, 2009, **1**, 552-556.
4. V. R. Stamenkovic, B. S. Mun, M. Arenz, K. J. J. Mayrhofer, C. A. Lucas, G. Wang, P. N. Ross and N. M. Markovic, Trends in electrocatalysis on extended and nanoscale Pt-bimetallic alloy surfaces, *Nat. Mater.*, 2007, **6**, 241-247.
5. L. Xiao, L. Zhuang, Y. Liu, J. Lu and H. D. Abruña, Activating Pd by Morphology Tailoring for Oxygen Reduction, *J. Am. Chem. Soc.*, 2009, **131**, 602-608.
6. Y. Liang, Y. Li, H. Wang, J. Zhou, J. Wang, T. Regier and H. Dai, Co<sub>3</sub>O<sub>4</sub> nanocrystals on graphene as a synergistic catalyst for oxygen reduction reaction, *Nat. Mater.*, 2011, **10**, 780-786.
7. Y. Li, W. Zhou, H. Wang, L. Xie, Y. Liang, F. Wei, J.-C. Idrobo, S. J. Pennycook and H. Dai, An oxygen reduction electrocatalyst based on carbon nanotube-graphene complexes, *Nat. Nanotechnol.*, 2012, **7**, 394-400.
8. V. R. Stamenkovic, B. Fowler, B. S. Mun, G. Wang, P. N. Ross, C. A. Lucas and N. M. Marković, Improved Oxygen Reduction Activity on Pt<sub>3</sub>Ni(111) via Increased Surface Site Availability, *Science*, 2007, **315**, 493.
9. Z. Pu, I. S. Amiinu, Z. Kou, W. Li and S. Mu, RuP<sub>2</sub>-Based Catalysts with Platinum-like Activity and Higher Durability for the Hydrogen Evolution Reaction at All pH Values, *Angew. Chem., Int. Ed.*, 2017, **56**, 11559-11564.
10. Z. Pu, J. Zhao, I. S. Amiinu, W. Li, M. Wang, D. He and S. Mu, A universal synthesis strategy for P-rich noble metal diphosphide-based electrocatalysts for the hydrogen evolution reaction, *Energy Environ. Sci.*, 2019, **12**, 952-957.
11. Z. Pu, R. Cheng, J. Zhao, Z. Hu, C. Li, W. Li, P. Wang, I. S. Amiinu, Z. Wang, W. Min, D. Chen and S. Mu, Anion-Modulated Platinum for High-Performance Multifunctional Electrocatalysis toward HER, HOR, and ORR, *iScience*, 2020, **23**, 101793.
12. K. C. Poon, D. C. L. Tan, T. D. T. Vo, B. Khezri, H. Su, R. D. Webster and H. Sato, Newly Developed Stepwise Electroless Deposition Enables a Remarkably Facile Synthesis of Highly Active and Stable Amorphous Pd Nanoparticle Electrocatalysts for Oxygen Reduction Reaction, *J. Am. Chem. Soc.*, 2014, **136**, 5217-5220.

13. M. Ren, Y. Kang, W. He, Z. Zou, X. Xue, D. L. Akins, H. Yang and S. Feng, Origin of performance degradation of palladium-based direct formic acid fuel cells, *Appl. Catal., B*, 2011, **104**, 49-53.
14. H. Erikson, A. Sarapuu, N. Alexeyeva, K. Tammeveski, J. Solla-Gullón and J. M. Feliu, Electrochemical reduction of oxygen on palladium nanocubes in acid and alkaline solutions, *Electrochim. Acta*, 2012, **59**, 329-335.
15. X. Chen, X. Zheng, W. Lin, D. Chen, Y. Zheng and L. Jiang, Adsorption property and catalytic performance over ordered mesoporous phosphorus-doped Pd-alumina catalysts, *Powder Technol.*, 2018, **338**, 869-877.
16. A. R. J. Kucernak, K. F. Fahy and V. N. N. Sundaram, Facile synthesis of palladium phosphide electrocatalysts and their activity for the hydrogen oxidation, hydrogen evolutions, oxygen reduction and formic acid oxidation reactions, *Catal. Today*, 2016, **262**, 48-56.
17. H. Erikson, A. Sarapuu, J. Kozlova, L. Matisen, V. Sammelselg and K. Tammeveski, Oxygen Electoreduction on Electrodeposited PdAu Nanoalloys, *Electrocatalysis*, 2015, **6**, 77-85.
18. J. H. Shim, J. Kim, C. Lee and Y. Lee, Porous Pd Layer-Coated Au Nanoparticles Supported on Carbon: Synthesis and Electrocatalytic Activity for Oxygen Reduction in Acid Media, *Chem. Mater.*, 2011, **23**, 4694-4700.
19. L. Jiang, A. Hsu, D. Chu and R. Chen, A highly active Pd coated Ag electrocatalyst for oxygen reduction reactions in alkaline media, *Electrochim. Acta*, 2010, **55**, 4506-4511.
20. H. Li, X. Jia, Q. Zhang and X. Wang, Metallic Transition-Metal Dichalcogenide Nanocatalysts for Energy Conversion, *Chem*, 2018, **4**, 1510-1537.
21. Z. He and W. Que, Molybdenum disulfide nanomaterials: Structures, properties, synthesis and recent progress on hydrogen evolution reaction, *Applied Materials Today*, 2016, **3**, 23-56.
22. X. Chia, A. Y. S. Eng, A. Ambrosi, S. M. Tan and M. Pumera, Electrochemistry of Nanostructured Layered Transition-Metal Dichalcogenides, *Chem. Rev.*, 2015, **115**, 11941-11966.
23. S. Stankovich, D. A. Dikin, G. H. B. Dommett, K. M. Kohlhaas, E. J. Zimney, E. A. Stach, R. D. Piner, S. T. Nguyen and R. S. Ruoff, Graphene-based composite materials, *Nature*, 2006, **442**, 282-286.
24. X. Li, X. Wang, L. Zhang, S. Lee and H. Dai, Chemically Derived, Ultrasoft Graphene Nanoribbon Semiconductors, *Science*, 2008, **319**, 1229.
25. H. Wang, Z. Lu, S. Xu, D. Kong, J. J. Cha, G. Zheng, P.-C. Hsu, K. Yan, D. Bradshaw, F. B. Prinz and Y. Cui, Electrochemical tuning of vertically aligned MoS nanofilms and its application in improving hydrogen evolution reaction, *Proc. Natl. Acad. Sci.*, 2013, **110**, 19701.
26. T. Y. Ma, S. Dai, M. Jaroniec and S. Z. Qiao, Graphitic Carbon Nitride Nanosheet–Carbon Nanotube Three-Dimensional Porous Composites as High-Performance Oxygen Evolution Electrocatalysts, *Angew. Chem., Int. Ed.*, 2014, **53**, 7281-7285.

View Article Online  
DOI: 10.1039/D0QM01113D

27. R. Zhao, Q. Li, X. Jiang, S. Huang, G. Fu and J.-M. Lee, Interface engineering in transition metal-based heterostructures for oxygen electrocatalysis, *Materials Chemistry Frontiers*, 2021, DOI: 10.1039/D0QM00729C.
28. E. Li, D. Wang, P. Fan, R. Zhang, Y.-Y. Zhang, G. Li, J. Mao, Y. Wang, X. Lin, S. Du and H.-J. Gao, Construction of bilayer PdSe<sub>2</sub> on epitaxial graphene, *Nano Res.*, 2018, **11**, 5858-5865.
29. A. D. Oyedele, S. Yang, L. Liang, A. A. Puretzky, K. Wang, J. Zhang, P. Yu, P. R. Pudasaini, A. W. Ghosh, Z. Liu, C. M. Rouleau, B. G. Sumpter, M. F. Chisholm, W. Zhou, P. D. Rack, D. B. Geohegan and K. Xiao, PdSe<sub>2</sub>: Pentagonal Two-Dimensional Layers with High Air Stability for Electronics, *J. Am. Chem. Soc.*, 2017, **139**, 14090-14097.
30. D. Qin, P. Yan, G. Ding, X. Ge, H. Song and G. Gao, Monolayer PdSe<sub>2</sub>: A promising two-dimensional thermoelectric material, *Scientific Reports*, 2018, **8**, 2764.
31. C. Long, Y. Liang, H. Jin, B. Huang and Y. Dai, PdSe<sub>2</sub>: Flexible Two-Dimensional Transition Metal Dichalcogenides Monolayer for Water Splitting Photocatalyst with Extremely Low Recombination Rate, *ACS Appl. Energy Mater.*, 2019, **2**, 513-520.
32. H. Li, C. Tsai, A. L. Koh, L. Cai, A. W. Contryman, A. H. Fragapane, J. Zhao, H. S. Han, H. C. Manoharan, F. Abild-Pedersen, J. K. Nørskov and X. Zheng, Activating and optimizing MoS<sub>2</sub> basal planes for hydrogen evolution through the formation of strained sulphur vacancies, *Nat. Mater.*, 2016, **15**, 48-53.
33. Y. Liu, C. Xiao, Z. Li and Y. Xie, Vacancy Engineering for Tuning Electron and Phonon Structures of Two-Dimensional Materials, *Adv. Energy Mater.*, 2016, **6**, 1600436.
34. H.-P. Komsa, J. Kotakoski, S. Kurasch, O. Lehtinen, U. Kaiser and A. V. Krasheninnikov, Two-Dimensional Transition Metal Dichalcogenides under Electron Irradiation: Defect Production and Doping, *Phys. Rev. Lett.*, 2012, **109**, 035503.
35. B. You, M. T. Tang, C. Tsai, F. Abild-Pedersen, X. Zheng and H. Li, Enhancing Electrocatalytic Water Splitting by Strain Engineering, *Adv. Mater.*, 2019, **31**, 1807001.
36. Y. Yu, S.-Y. Huang, Y. Li, S. N. Steinmann, W. Yang and L. Cao, Layer-Dependent Electrocatalysis of MoS<sub>2</sub> for Hydrogen Evolution, *Nano Lett.*, 2014, **14**, 553-558.
37. J. Xie, H. Zhang, S. Li, R. Wang, X. Sun, M. Zhou, J. Zhou, X. W. Lou and Y. Xie, Defect-Rich MoS<sub>2</sub> Ultrathin Nanosheets with Additional Active Edge Sites for Enhanced Electrocatalytic Hydrogen Evolution, *Adv. Mater.*, 2013, **25**, 5807-5813.
38. Q. Gong, L. Cheng, C. Liu, M. Zhang, Q. Feng, H. Ye, M. Zeng, L. Xie, Z. Liu and Y. Li, Ultrathin MoS<sub>2</sub>(1-x)Se<sub>2x</sub> Alloy Nanoflakes For Electrocatalytic Hydrogen Evolution Reaction, *ACS Catal.*, 2015, **5**, 2213-2219.
39. L. S. Bezerra and G. Maia, Developing efficient catalysts for the OER and ORR

View Article Online  
DOI: 10.1039/D0QM01113D

- using a combination of Co, Ni, and Pt oxides along with graphene nanoribbons and NiCo<sub>2</sub>O<sub>4</sub>, *J. Mater. Chem. A*, 2020, **8**, 17691-17705.
40. K. J. Koski, J. J. Cha, B. W. Reed, C. D. Wessells, D. Kong and Y. Cui, High-Density Chemical Intercalation of Zero-Valent Copper into Bi<sub>2</sub>Se<sub>3</sub> Nanoribbons, *J. Am. Chem. Soc.*, 2012, **134**, 7584-7587.
  41. E. Yoo, J. Kim, E. Hosono, H.-s. Zhou, T. Kudo and I. Honma, Large Reversible Li Storage of Graphene Nanosheet Families for Use in Rechargeable Lithium Ion Batteries, *Nano Lett.*, 2008, **8**, 2277-2282.
  42. K. J. Koski, C. D. Wessells, B. W. Reed, J. J. Cha, D. Kong and Y. Cui, Chemical Intercalation of Zerovalent Metals into 2D Layered Bi<sub>2</sub>Se<sub>3</sub> Nanoribbons, *J. Am. Chem. Soc.*, 2012, **134**, 13773-13779.
  43. Y. Guo, C. Feng, S. Wang, Y. Xie, C. Guo, Z. Liu, N. Akram, Y. Zhang, Y. Zhao and J. Wang, Construction of planar-type defect-engineered metal-organic frameworks with both mixed-valence sites and copper-ion vacancies for photocatalysis, *J. Mater. Chem. A*, 2020, **8**, 24477-24485.
  44. J. Xia, J. Wang, D. Chao, Z. Chen, Z. Liu, J.-L. Kuo, J. Yan and Z. X. Shen, Phase evolution of lithium intercalation dynamics in 2H-MoS<sub>2</sub>, *Nanoscale*, 2017, **9**, 7533-7540.
  45. R. Kappera, D. Voiry, S. E. Yalcin, B. Branch, G. Gupta, A. D. Mohite and M. Chhowalla, Phase-engineered low-resistance contacts for ultrathin MoS<sub>2</sub> transistors, *Nat. Mater.*, 2014, **13**, 1128-1134.
  46. D. Voiry, M. Salehi, R. Silva, T. Fujita, M. Chen, T. Asefa, V. B. Shenoy, G. Eda and M. Chhowalla, Conducting MoS<sub>2</sub> Nanosheets as Catalysts for Hydrogen Evolution Reaction, *Nano Lett.*, 2013, **13**, 6222-6227.
  47. H. Deng, C. Zhang, Y. Xie, T. Tumlin, L. Giri, S. P. Karna and J. Lin, Laser induced MoS<sub>2</sub>/carbon hybrids for hydrogen evolution reaction catalysts, *J. Mater. Chem. A*, 2016, **4**, 6824-6830.
  48. P. Connor, J. Schuch, B. Kaiser and W. Jaegermann, The Determination of Electrochemical Active Surface Area and Specific Capacity Revisited for the System MnOx as an Oxygen Evolution Catalyst, *Zeitschrift für Physikalische Chemie*, 2020, **234**, 979-994.
  49. D. Chen, Q. Tao, L. W. Liao, S. X. Liu, Y. X. Chen and S. Ye, Determining the Active Surface Area for Various Platinum Electrodes, *Electrocatalysis*, 2011, **2**, 207.
  50. M. L. Tremblay, M. H. Martin, C. Lebouin, A. Lasia and D. Guay, Determination of the real surface area of powdered materials in cavity microelectrodes by electrochemical impedance spectroscopy, *Electrochim. Acta*, 2010, **55**, 6283-6291.
  51. B. Łosiewicz, M. Martin, C. Lebouin and A. Lasia, Kinetics of hydrogen underpotential deposition at ruthenium in acidic solutions, *Journal of Electroanalytical Chemistry*, 2010, **649**, 198-205.
  52. G. Kresse and J. Furthmüller, Efficient iterative schemes for ab initio total-energy calculations using a plane-wave basis set, *Phys. Rev. B*, 1996, **54**, 11169-

- 11186.
53. J. P. Perdew, K. Burke and Y. Wang, Generalized gradient approximation for the exchange-correlation hole of a many-electron system, *Phys. Rev. B*, 1996, **54**, 16533-16539.
54. J. P. Perdew, K. Burke and M. Ernzerhof, Generalized Gradient Approximation Made Simple, *Phys. Rev. Lett.*, 1996, **77**, 3865-3868.
55. P. E. Blöchl, Projector augmented-wave method, *Phys. Rev. B*, 1994, **50**, 17953-17979.
56. S. Grimme, Semiempirical GGA-type density functional constructed with a long-range dispersion correction, *J. Comput. Chem.*, 2006, **27**, 1787-1799.
57. K. Mathew, R. Sundararaman, K. Letchworth-Weaver, T. A. Arias and R. G. Hennig, Implicit solvation model for density-functional study of nanocrystal surfaces and reaction pathways, *The Journal of Chemical Physics*, 2014, **140**, 084106.
58. Y. Guo, Z. Dai, J. Lu, X. Zeng, Y. Yuan, X. Bi, L. Ma, T. Wu, Q. Yan and K. Amine, Lithiation-Induced Non-Noble Metal Nanoparticles for Li-O<sub>2</sub> Batteries, *ACS Appl. Mater. Interfaces*, 2019, **11**, 811-818.
59. D. Balzar, X-Ray Diffraction Line Broadening: Modeling and Applications to High-T(c) Superconductors, *J Res Natl Inst Stand Technol*, 1993, **98**, 321-353.
60. C. Yan, Z. Fang, C. Lv, X. Zhou, G. Chen and G. Yu, Significantly Improving Lithium-Ion Transport via Conjugated Anion Intercalation in Inorganic Layered Hosts, *ACS Nano*, 2018, **12**, 8670-8677.
61. X. Zheng, W. Chen, G. Wang, Y. Yu, S. Qin, J. Fang, F. Wang and X.-A. Zhang, The Raman redshift of graphene impacted by gold nanoparticles, *AIP Advances*, 2015, **5**, 057133.
62. C. G. Freyschlag and R. J. Madix, Precious metal magic: catalytic wizardry, *Materials Today*, 2011, **14**, 134-142.
63. T. Muroi, in *Noble Metals*, ed. Y.-H. Su, IntechOpen, 2012, DOI: 10.5772/34249.
64. S. F. Parker, S. Mukhopadhyay, M. Jiménez-Ruiz and P. W. Albers, Adsorbed States of Hydrogen on Platinum: A New Perspective, *Chemistry – A European Journal*, 2019, **25**, 6496-6499.
65. N. Weidler, J. Schuch, F. Knaus, P. Stenner, S. Hoch, A. Maljusch, R. Schäfer, B. Kaiser and W. Jaegermann, X-ray Photoelectron Spectroscopic Investigation of Plasma-Enhanced Chemical Vapor Deposited NiO<sub>x</sub>, NiO<sub>x</sub>(OH)<sub>y</sub>, and CoNiO<sub>x</sub>(OH)<sub>y</sub>: Influence of the Chemical Composition on the Catalytic Activity for the Oxygen Evolution Reaction, *J. Phys. Chem. C*, 2017, **121**, 6455-6463.
66. J. Hu, L. Shi, Q. Liu, H. Huang and T. Jiao, Improved oxygen reduction activity on silver-modified LaMnO<sub>3</sub>-graphene via shortens the conduction path of adsorbed oxygen, *RSC Adv.*, 2015, **5**, 92096-92106.
67. S. Maruyama, T. Fukutsuka, K. Miyazaki, Y. Abe, N. Yoshizawa and T. Abe, Lithium-ion intercalation and deintercalation behaviors of graphitized carbon

View Article Online  
DOI: 10.1039/D0QM01113D



- nanospheres, *J. Mater. Chem. A*, 2018, **6**, 1128-1137.
68. A. Wang, S. Kadam, H. Li, S. Shi and Y. Qi, Review on modeling of the anode solid electrolyte interphase (SEI) for lithium-ion batteries, *npj Comput. Mater.*, 2018, **4**, 15.
  69. S. J. An, J. Li, C. Daniel, D. Mohanty, S. Nagpure and D. L. Wood, The state of understanding of the lithium-ion-battery graphite solid electrolyte interphase (SEI) and its relationship to formation cycling, *Carbon*, 2016, **105**, 52-76.
  70. J. Huang, X. Guo, X. Du, X. Lin, J.-Q. Huang, H. Tan, Y. Zhu and B. Zhang, Nanostructures of solid electrolyte interphases and their consequences for micro-sized Sn anodes in sodium ion batteries, *Energy Environ. Sci.*, 2019, **12**, 1550-1557.
  71. T. Zhan, X. Liu, S. Lu and W. Hou, Nitrogen doped NiFe layered double hydroxide/reduced graphene oxide mesoporous nanosphere as an effective bifunctional electrocatalyst for oxygen reduction and evolution reactions, *Appl. Catal., B*, 2017, **205**, 551-558.
  72. C. Bianchini and P. K. Shen, Palladium-Based Electrocatalysts for Alcohol Oxidation in Half Cells and in Direct Alcohol Fuel Cells, *Chem. Rev.*, 2009, **109**, 4183-4206.
  73. S. Siwal, S. Matseke, S. Mpelane, N. Hooda, D. Nandi and K. Mallick, Palladium-polymer nanocomposite: An anode catalyst for the electrochemical oxidation of methanol, *Int. J. Hydrogen Energy*, 2017, **42**, 23599-23605.
  74. M. I. Prodromidis, E. M. Zahran, A. G. Tzakos and L. G. Bachas, Preorganized composite material of polyaniline-palladium nanoparticles with high electrocatalytic activity to methanol and ethanol oxidation, *Int. J. Hydrogen Energy*, 2015, **40**, 6745-6753.
  75. C. Souillard, X. Rocquefelte, P. E. Petit, M. Evain, S. Jobic, J. P. Itié, P. Munsch, H. J. Koo and M. H. Whangbo, Experimental and Theoretical Investigation on the Relative Stability of the PdS<sub>2</sub>- and Pyrite-Type Structures of PdSe<sub>2</sub>, *Inorg. Chem.*, 2004, **43**, 1943-1949.
  76. R. Dronskowski and P. E. Bloechl, Crystal orbital Hamilton populations (COHP): energy-resolved visualization of chemical bonding in solids based on density-functional calculations, *J. Phys. Chem.*, 1993, **97**, 8617-8624.
  77. Y. Zhao, J. Qiao, P. Yu, Z. Hu, Z. Lin, S. P. Lau, Z. Liu, W. Ji and Y. Chai, Extraordinarily Strong Interlayer Interaction in 2D Layered PtS<sub>2</sub>, *Adv. Mater.*, 2016, **28**, 2399-2407.
  78. H. Huang, X. Fan, D. J. Singh and W. Zheng, Modulation of Hydrogen Evolution Catalytic Activity of Basal Plane in Monolayer Platinum and Palladium Dichalcogenides, *ACS Omega*, 2018, **3**, 10058-10065.
  79. J. K. Nørskov, J. Rossmeisl, A. Logadottir, L. Lindqvist, J. R. Kitchin, T. Bligaard and H. Jónsson, Origin of the Overpotential for Oxygen Reduction at a Fuel-Cell Cathode, *J. Phys. Chem. B*, 2004, **108**, 17886-17892.
  80. R. Lawler, J. Cho, H. C. Ham, H. Ju, S. W. Lee, J. Y. Kim, J. I. Choi and S. S. Jang, CeO<sub>2</sub>(111) Surface with Oxygen Vacancy for Radical Scavenging: A

Density Functional Theory Approach, *J. Phys. Chem. C*, 2020, **124**, 20950-20959. [View Article Online](#)  
DOI: 10.1039/D0QM01113D